Electronic Supplementary Information for:

INCREASED SPATIAL RANDOMNESS AND DISORDER OF NUCLEATES IN DARK-PHASE ELECTRODEPOSITION LEAD TO INCREASED SPATIAL ORDER AND PATTERN FIDELITY IN PHOTOTROPICALLY GROWN SE-TE ELECTRODEPOSITS

ETHAN SIMONOFF[†], LORENZO X. VAN MUÑOZ[†], NATHAN S. LEWIS[†,l,*]

[†]Division of Chemistry and Chemical Engineering. 127-72, 210 Noyes Laboratory

[l]Beckman Institute

California Institute of Technology

Pasadena, CA 91125

*Corresponding Author: nslewis@caltech.edu

Contents

SI. **Experimental methods and materials**

Unless otherwise noted, all experiments were performed following nominally identical procedures from our previously reported work.[1] This included chemicals and materials used, equipment used, electrode fabrication procedures, electrochemical configuration, optical configuration, sample preparation, and image acquisition as was described in Section S2 of the Electronic Supplementary Information.
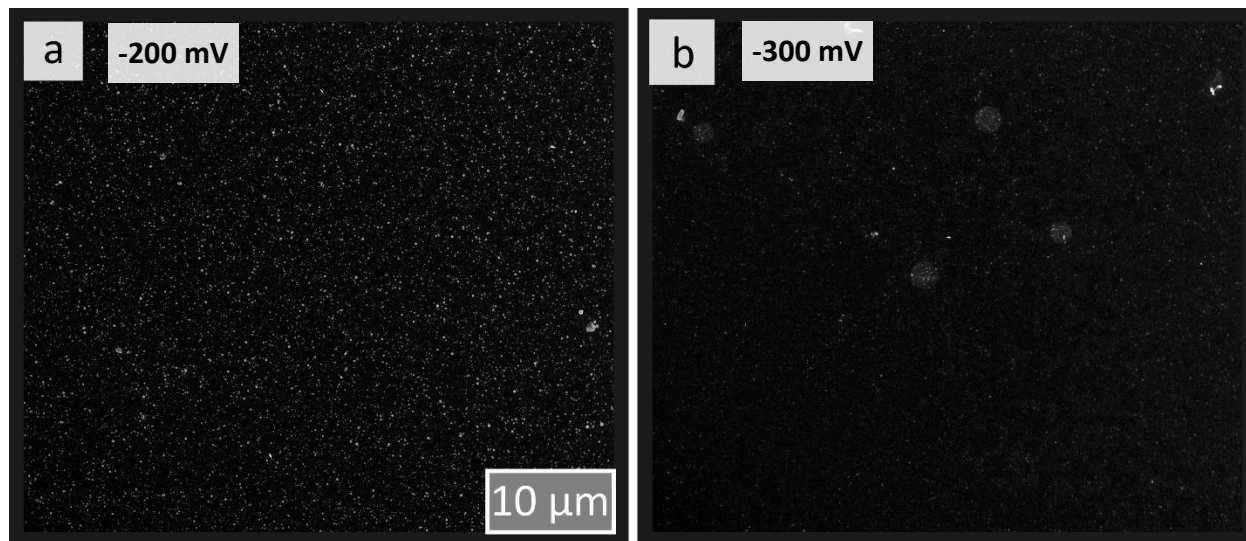
SII. Examples of low-magnification images

Figure S1: Low-magnification SEM images of photoelectrodeposited Se-Te films shown in Figure 1 grown on n^+-Si at a charge density of -3.75 mC cm^{-2} using vertically polarized λ = 927 nm illumination at a power density of 53 mW cm^{-2}. (a) deposited at relatively more positive deposition potential, (b) deposited at relatively more negative deposition potentials vs. Ag/AgCl. These SEM images were obtained at a magnification of 6250 X and a resolution of 4096 x 3536 pixels, which corresponded to ~85.8 pixels μm^{-1}. The applied deposition potentials are reported versus a reference potential rather than as an overpotential to the reversible potential. The reversible potential is not known for the following reaction:

$$x\text{Se}^{4+} + y\text{Te}^{4+} + (x + y)8\text{e}^- \rightleftarrows \text{Se}_x\text{-Te}_y$$
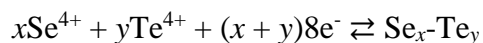
The solid-liquid interface changes dramatically during deposition of the Se-Te alloy producing an accompanying response in the open-circuit potential (OCP), complicating the reporting of an overpotential to the reversible potential for this reaction. Additionally, the OCP is observed to depend on substrate choice and the solid-solid or solid-liquid junctions formed. Accordingly, we

prefer reporting the applied deposition potential (used in a potentiostatic deposition experiment) versus a reference potential.
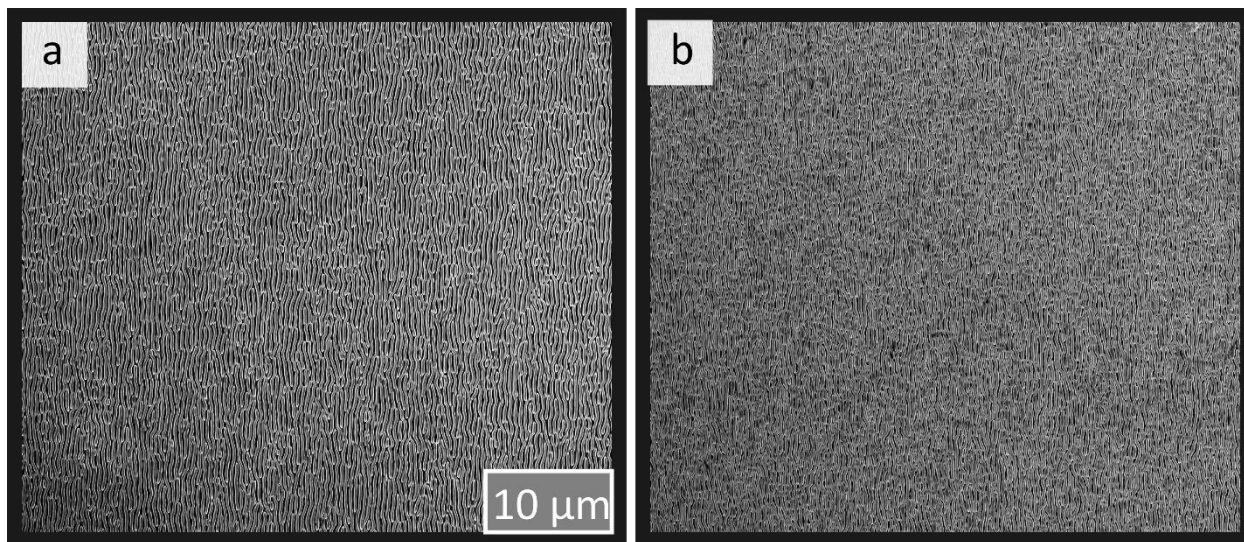
Figure S2: Low-magnification SEM images of photoelectrodeposited Se-Te films that were deposited at a charge density of -750 mC cm^{-2} using vertically polarized $\lambda = 927$ nm illumination at a power density of 53 mW cm^{-2} on (a) p^{+}-Si and (b) n^{+}-Si, corresponding to Figure 2(j) and (t), respectively. These SEM images were obtained at a magnification of 6250 X and a resolution of 4096 x 3536 pixels, which corresponded to ~85.8 pixels μm^{-1}.

SIII. Reproducibility
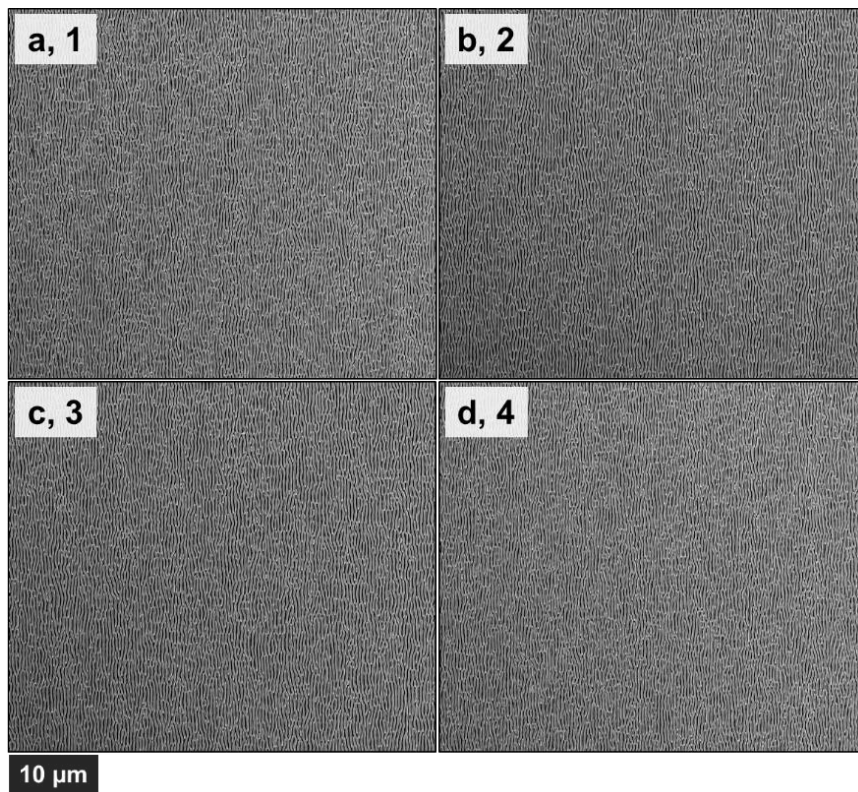
Spot #	Period (nm)	Vertical FWHM (°)
1	370.4	31.7
2	367.1	28.0
3	371.3	29.6
4	357.1	30.4
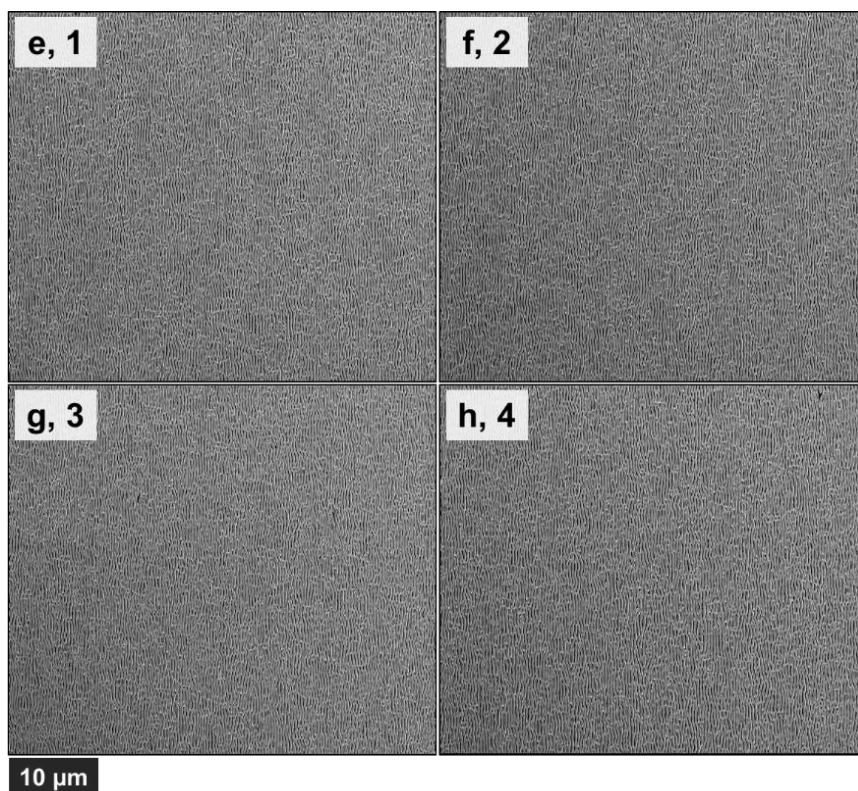
Spot #	Period (nm)	Vertical FWHM (°)
1	322.8	33.7
2	328.5	33.0
3	323.8	34.6
4	332.8	32.9
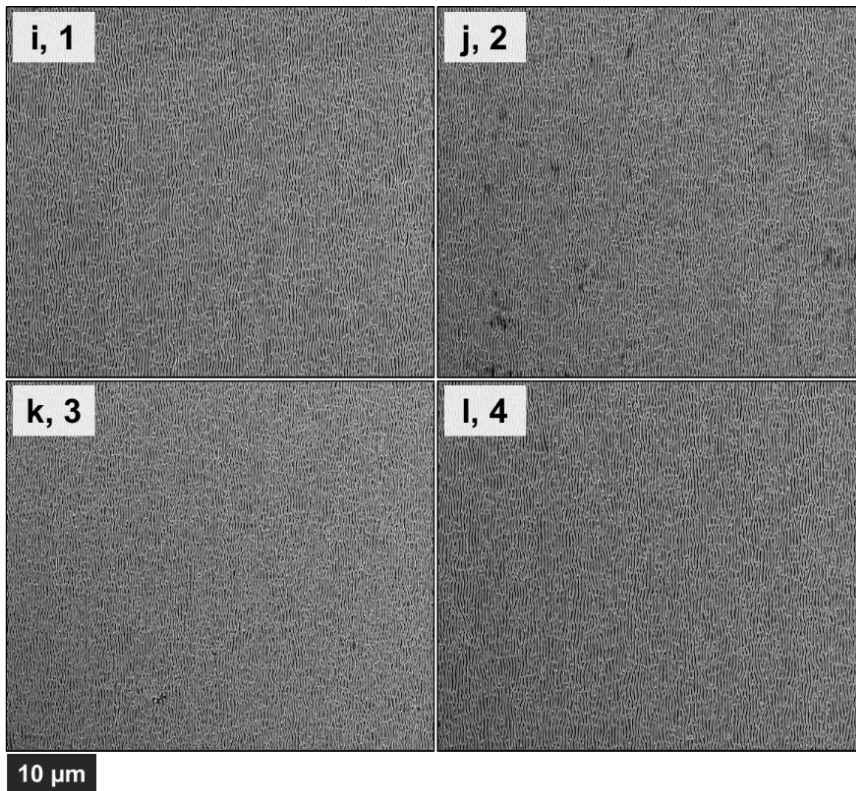
Spot #	Period (nm)	Vertical FWHM (°)
1	345.9	30.2
2	336.6	32.4
3	329.1	38.7
4	352.7	30.5
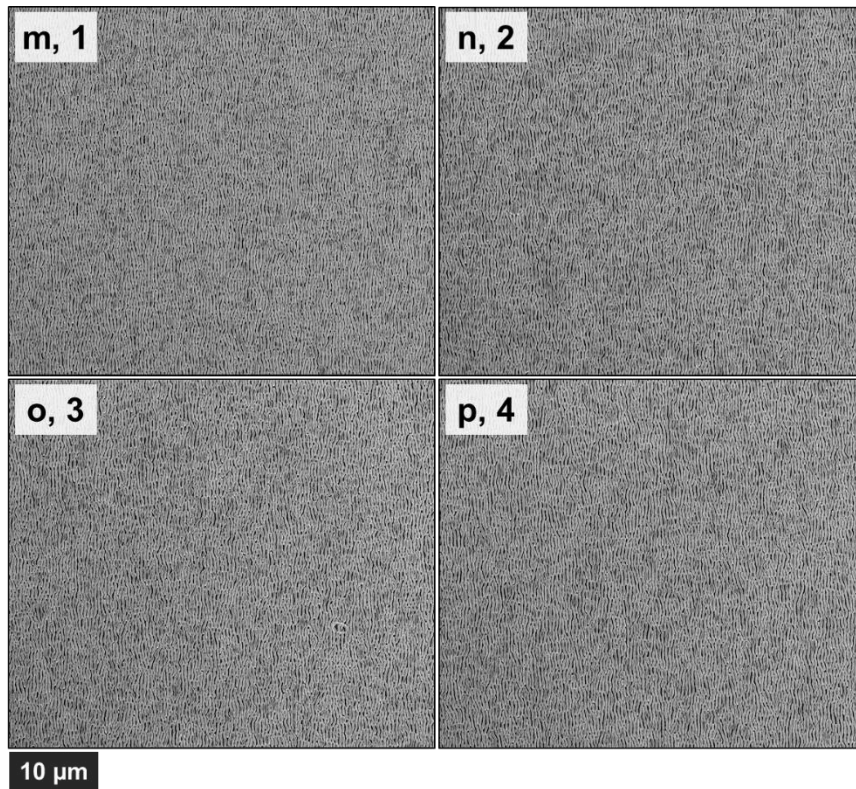
Spot #	Period (nm)	Vertical FWHM (°)
1	370.6	38.7
2	369.3	38.6
3	382.1	43.6
4	374.8	38.8
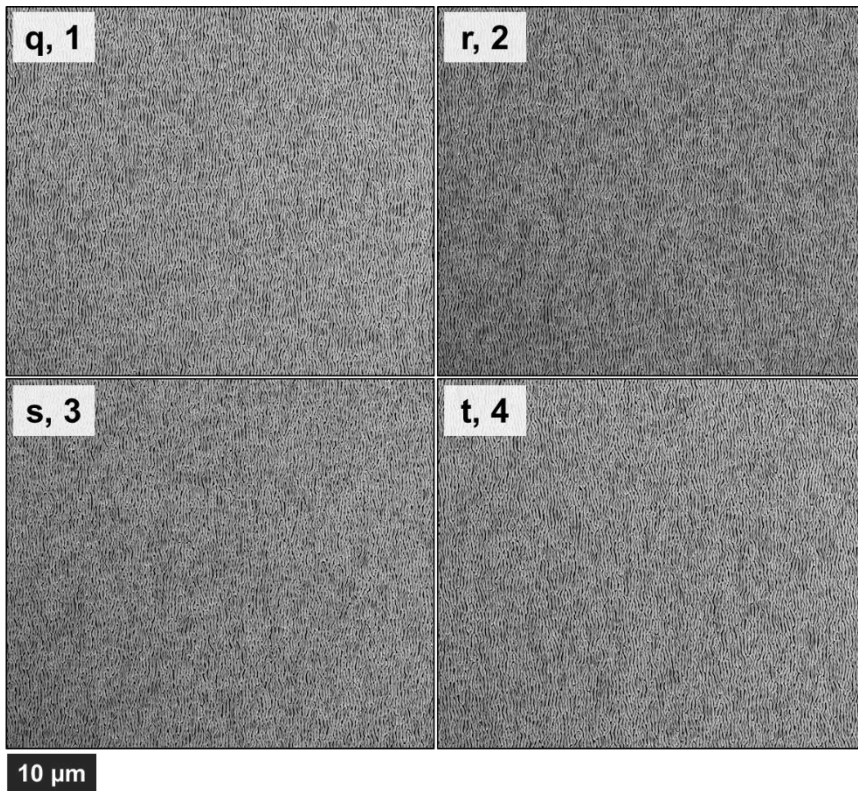
Spot #	Period (nm)	Vertical FWHM (°)
1	368.6	41.6
2	373.8	41.8
3	368.3	47.1
4	373.1	42.4
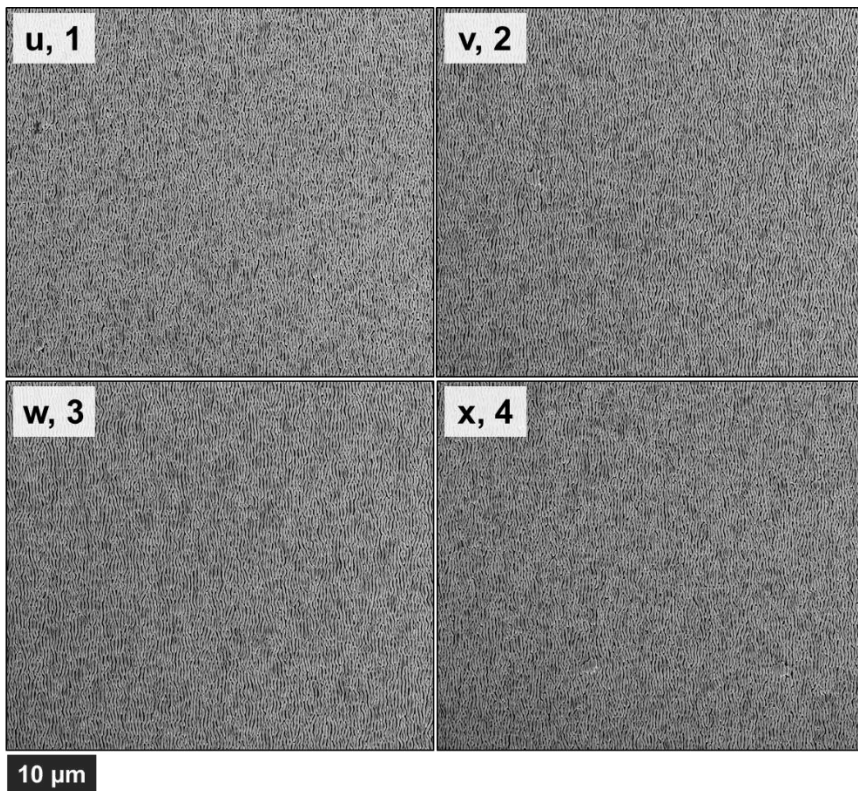
Spot #	Period (nm)	Vertical FWHM (°)
1	360.8	46.7
2	372.0	42.6
3	372.2	41.2
4	367.1	47.3

Figure S3: Low-magnification SEM images of Se-Te films that were photoelectrodeposited at a charge density of -750 mC cm^{-2} using vertically polarized λ = 927 nm illumination at a power density of 53 mW cm^{-2} on (a-l) p^{+}-Si and (m-x) n^{+}-Si. These SEM images were obtained at a magnification of 6250 X and a resolution of 4096 x 35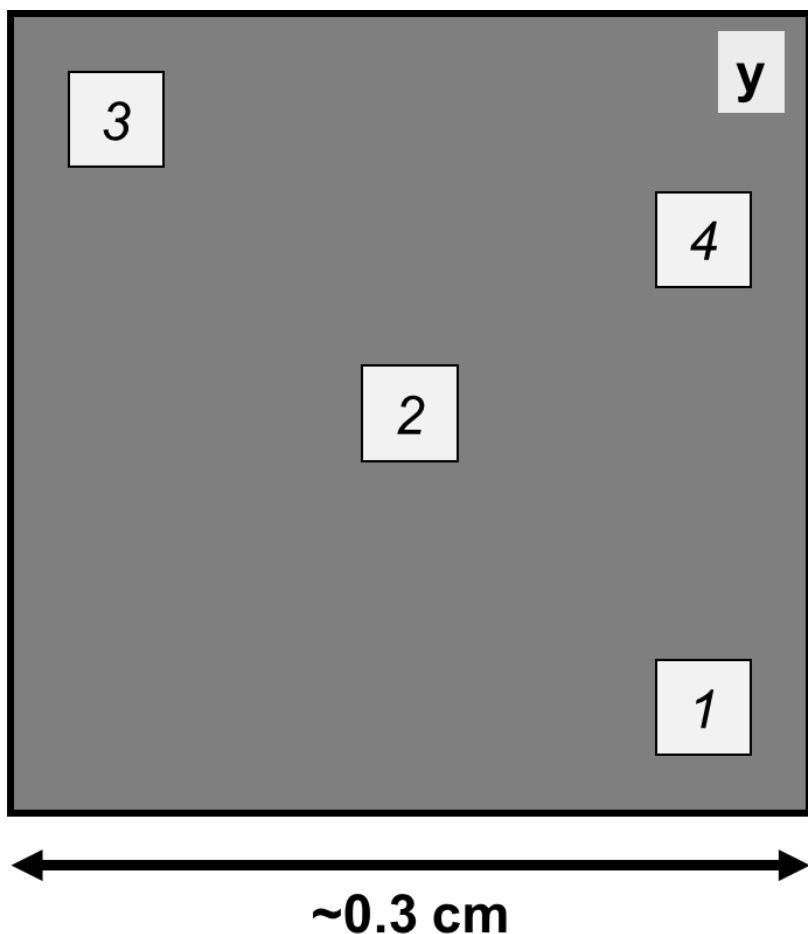36 pixels, which corresponded to ~85.8 pixels μm^{-1}. Each set of four images (a-d, e-h, etc.) corresponds to various spots on a single phototropic Se-Te film; approximate locations of 1, 2, 3, or 4 are noted in (y). Pattern fidelity information is given in adjacent tables, showing that patterns generally displayed excellent reproducibility across macroscopic length scales.

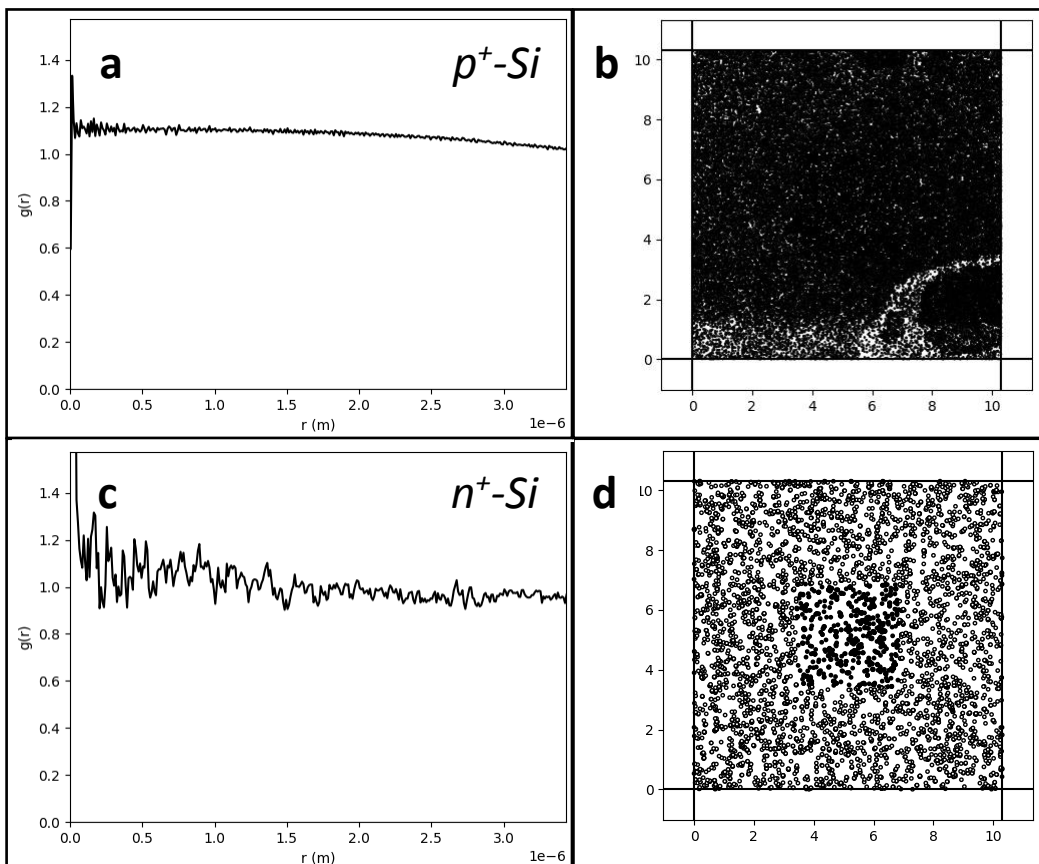## SIV. Pair-correlation function (PCF) examples

Figure S4: Results of a pair-correlation function (PCF) analysis performed on data obtained from the images in (a), (b) Figure 1a and (c), (d) Figure 1c, corresponding to Se-Te nucleates on p$^+$-Si and n$^+$-Si, respectively. PCF plots in (a), (c) were obtained via a pair-correlation Python script[2] provided via GNU General Public License v3.0. Particle coordinate data in (b), (d) were obtained using grain analysis in the Gwyddion software package (www.gwyddion.net). Axis units in (b), (d) are in μm; test points used in PCF analysis are confined to a central square region comprising 1/9th of the total area. The PCF analysis of nucleates on p$^+$-Si shows a higher degree of randomness in the distribution of particles, as observed in the smooth and isotropic plot. Conversely, the PCF analysis of nucleates on n$^+$-Si shows more disorder in the PCF plot, corresponding to less randomly

distributed particles. PCF analysis weights all particles equally through a binary input of coordinate data either containing or not containing nucleates. FT analysis provides a gradient of weighting based on white value in the imaged nucleates. We believe that FT analysis is a more robust method for characterizing certain film morphologies in which exact nucleate coordinates are not obvious or easily recognized. For instance, in many of the p^+-Si nucleates, film morphologies are closer to thin films than distributions of distinct particles, thus making PCF analysis difficult and prone to error generated during the grain analysis step. Given its broader applicability, FT is our preferred method of analysis for assessing the distribution of Se-Te nucleates on all substrates.
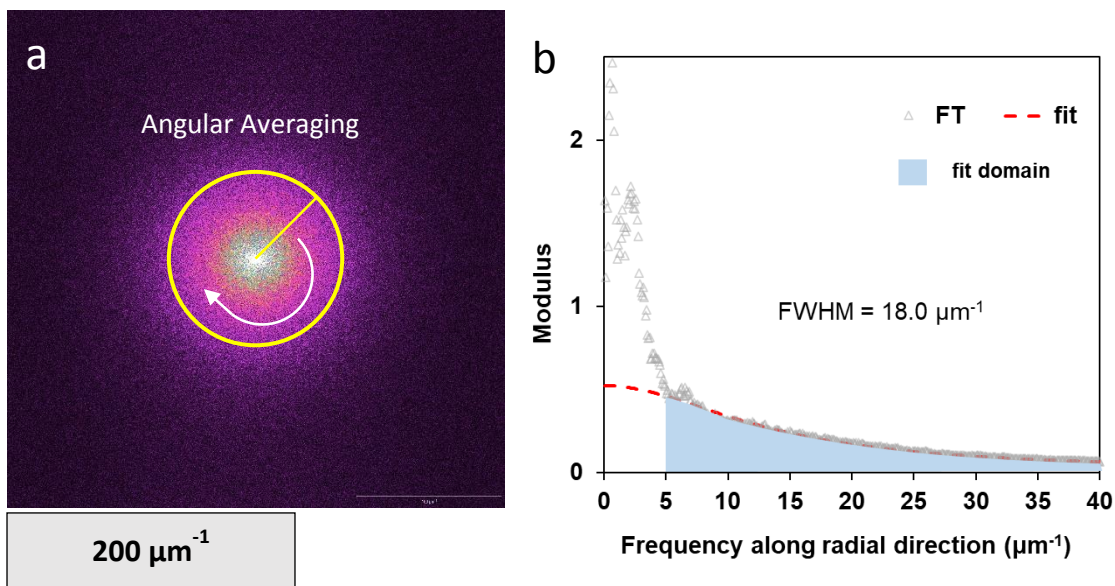
SV. Peak-fitting methodologies

Figure S5: To determine the nucleate spacing, SEM images were obtained of samples deposited at a charge density of -3.75 mC cm^{-2} at 50 k magnification and at a resolution of 2048 x 1768 pixels, which corresponded to ~171.6 pixels μm^{-1}. As a representative example, (a) shows a 2D FT spectrum of one of these images. To obtain the nucleate spacing, the 2D FT was angularly averaged around the origin to obtain the radial spectrum shown in (b). To minimize overlap from the centroid DC peak of the 2D FT spectrum, the decay of the radial spectrum was fit using a Lorentzian function in which the mean of the distribution was fixed to the origin and the fit domain range was fixed between 5 μm^{-1} and 100 μm^{-1}. The peak half-width at half maximum (HWHM) of the resulting fit was inverted to obtain the nucleate spacing used as a figure-of-merit as reported in the main text. Larger HWHM values indicated smaller nucleate spacing.
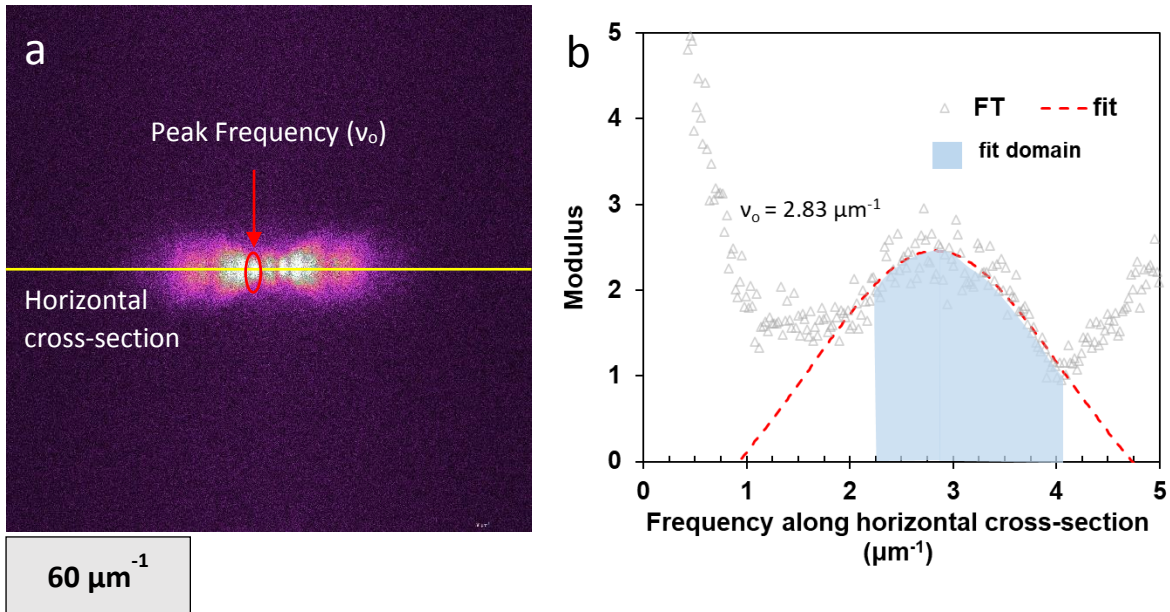
Figure S6: 2D FT spectra of large-area SEM images, such as those in Figure S2, were used to obtain the average pattern period measurements reported in Figure 3 of the main text. An example is provided in (a), showing symmetric lobes along the horizontal axis, perpendicular to the axis of polarization. A horizontal cross section through the origin, integrated over 30 pixels vertically, gave the profile in (b). A Lorentzian function was fit to the primary peak in the obtained spectrum. The domain of the fit was chosen to minimize the residual between the fit and the data. The center frequency of the peak, v_o, was recorded. The inverse of v_o corresponded to the average primary pattern period.
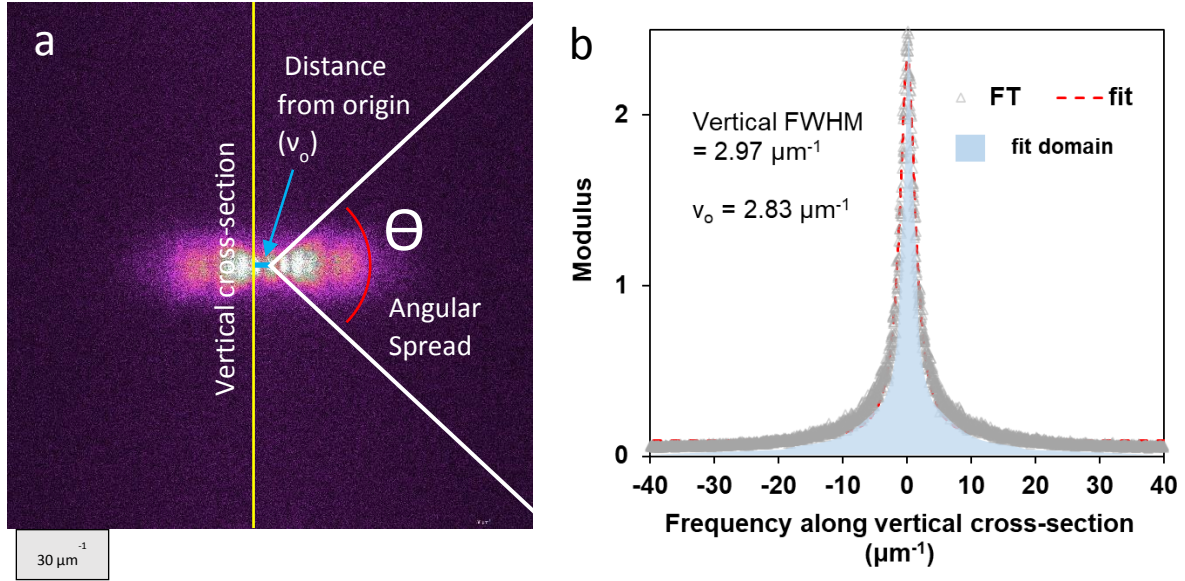
Figure S7: 2D FT spectra of large-area SEM images, such as those in Figure S2, were used to obtain the angular FWHM measurements reported in Figure 3 of the main text. An example is provided in (a). A vertical cross section through v_o as obtained in Figure S6, integrated over 30 pixels horizontally, gave the profile in (b). A Lorentzian function was fit to this peak in the obtained spectrum, with the entire profile included in the fit domain. The peak full-width at half maximum (FWHM) was obtained, in μm^{-1}, and converted to radial coordinates using the formula in Equation S1. Narrower FWHM corresponded to higher pattern fidelity.

Equation S1:   Vertical FWHM (^{o}) $=$ $2\,tan^{-1}\left(\dfrac{\text{Vertical FWHM}}{2\cdot v_o}\right)$

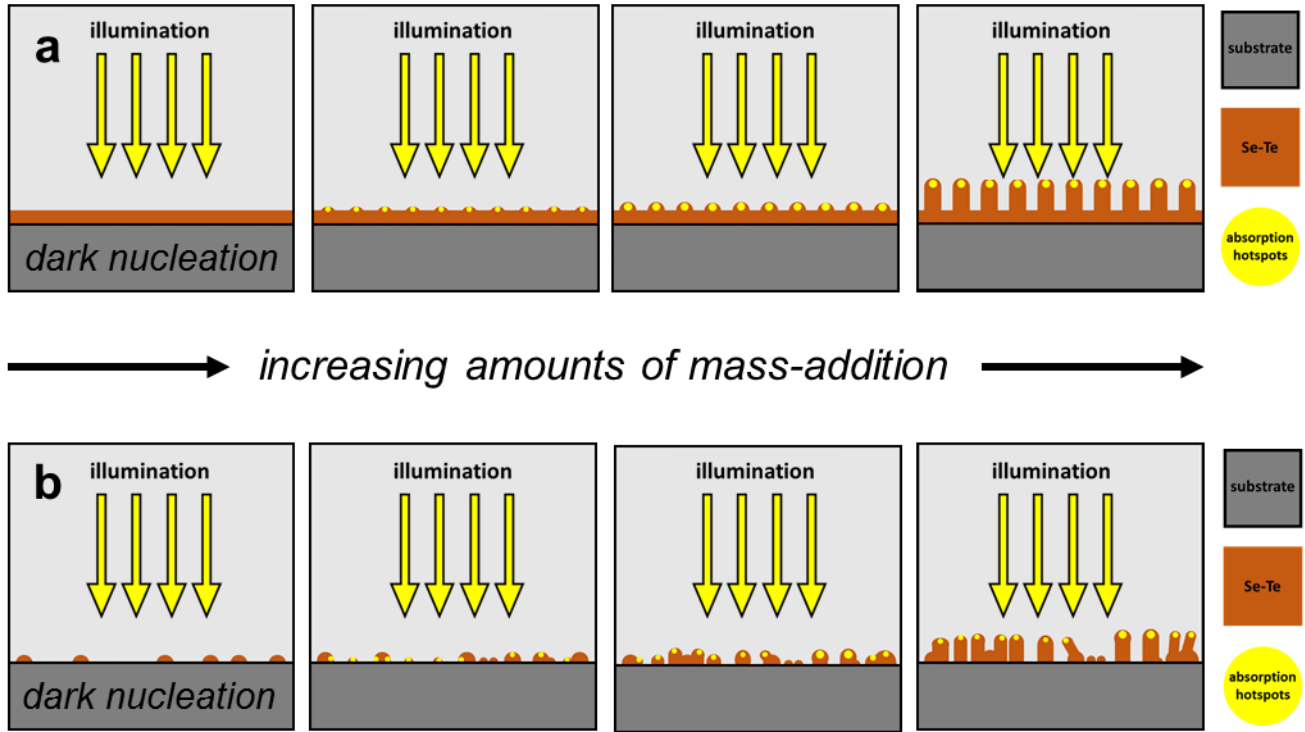## SVI. Schemes for phototropic growth mechanism

Figure S8: Schemes showing the process by which an initially dark Se-Te nucleation results in highly ordered, periodic lamellae when illuminated with polarized light with a photon energy above the optical bandgap of Se-Te. Scheme in (a) demonstrates phototropic growth wherein dark phase nucleation resembles a thin, continuous film of Se-Te material. The panels in Scheme (b) depict phototropic growth wherein dark phase nucleation is slow, progressive, and discontinuous. A more random and continuous distribution of optical dipole scatterers, i.e. nucleated Se-Te particles or surface roughness on a thin Se-Te film (Scheme a), results in higher fidelity pattern formation regardless of the direction or wavelength of the incident light beam. This property derives from maximization of mass addition due to local light absorption over the duration of pattern formation. In contrast, a discontinuous or sparse distribution of optical dipole scatterers results in a delay and misregistry in phototropically grown pattern formation. Dislocations in the

phototropically grown film thus result from discontinuity in the nucleation morphology. Conversely, discontinuity in nucleated films directly results in pattern defects.
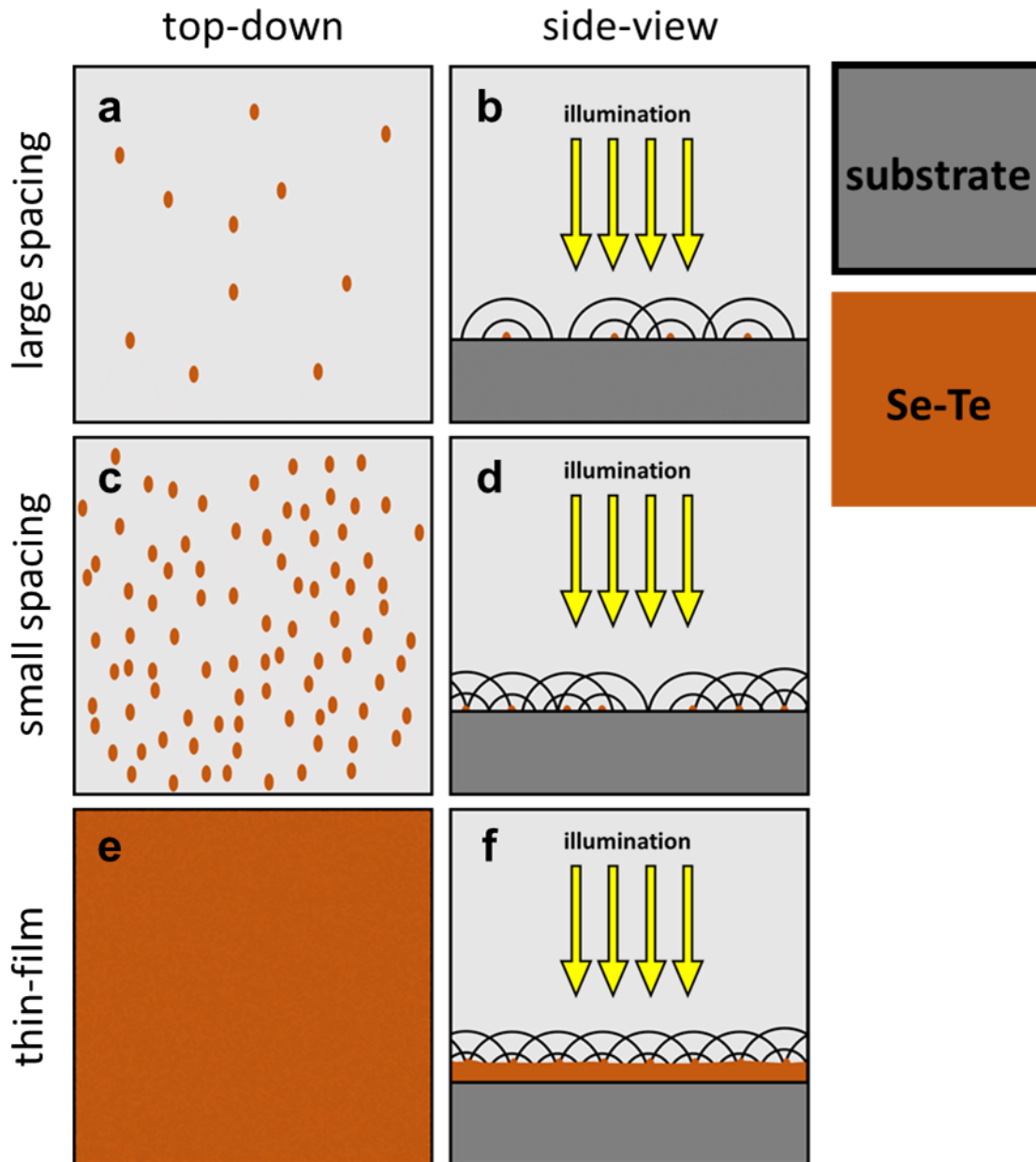
Figure S9: Schemes showing the interaction of scattered light waves with nucleated Se-Te optical dipole scatterers. Diagrams in (a), (b) show an initial Se-Te nucleation morphology characterized by large nucleate spacing; diagrams in (c), (d) show an initial Se-Te nucleation morphology characterized by small nucleate spacing; diagrams in (e), (f) show an initially thin-film Se-Te nucleation morphology. In the case of (e), (f), a thin-film nucleation results in the highest tolerance for overlap between mass availability and scattered-wave intensity. In the case of (c), (d), gaps in

nucleation spacing can lead to conditions in which optical dipole scatterers are not in collective resonance. In the case of (a), (b), larger nucleation spacing further increases the chances of dipole-scatterers being out of collective resonance for a given excitation wavelength and direction of optical incidence. The coincidence of mass and scattered-wave intensity is a prerequisite for a corresponding coincidence of scattered-wave intensity and local light absorption. Furthermore, local light absorption is proportional to mass addition in phototropic growth, hence the conditions that produce better overlap between mass and scattered-wave intensity maximize light-directed growth, consequently producing higher anisotropy - and higher fidelity - in phototropic films.

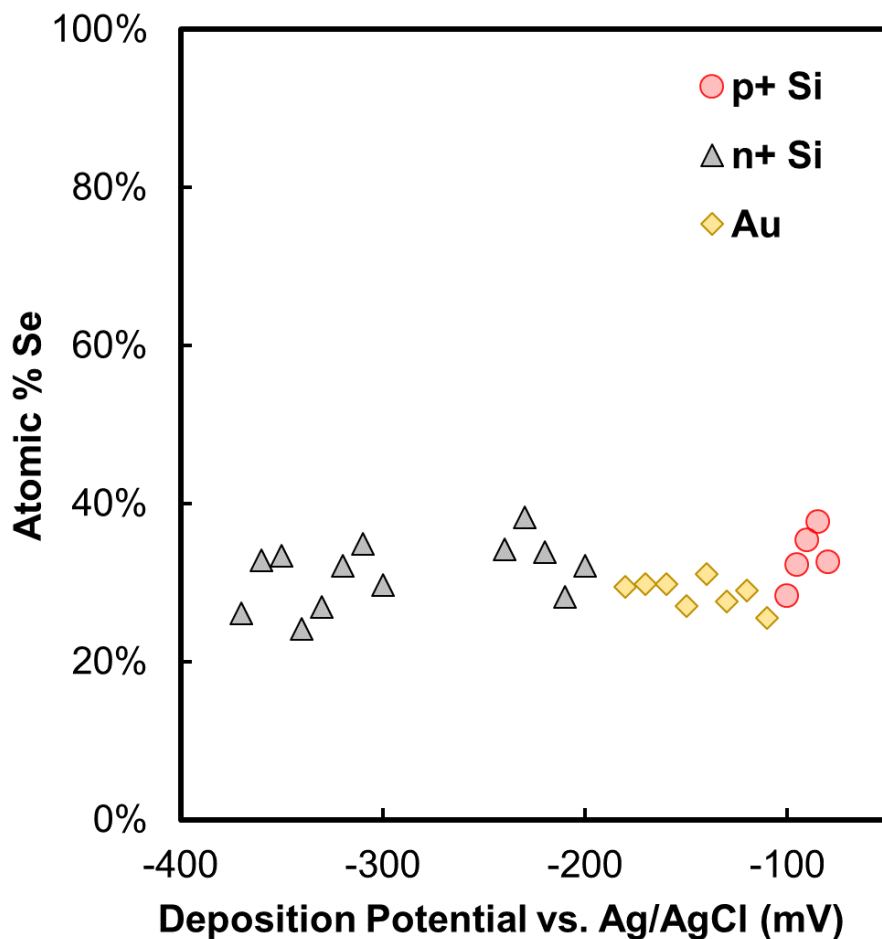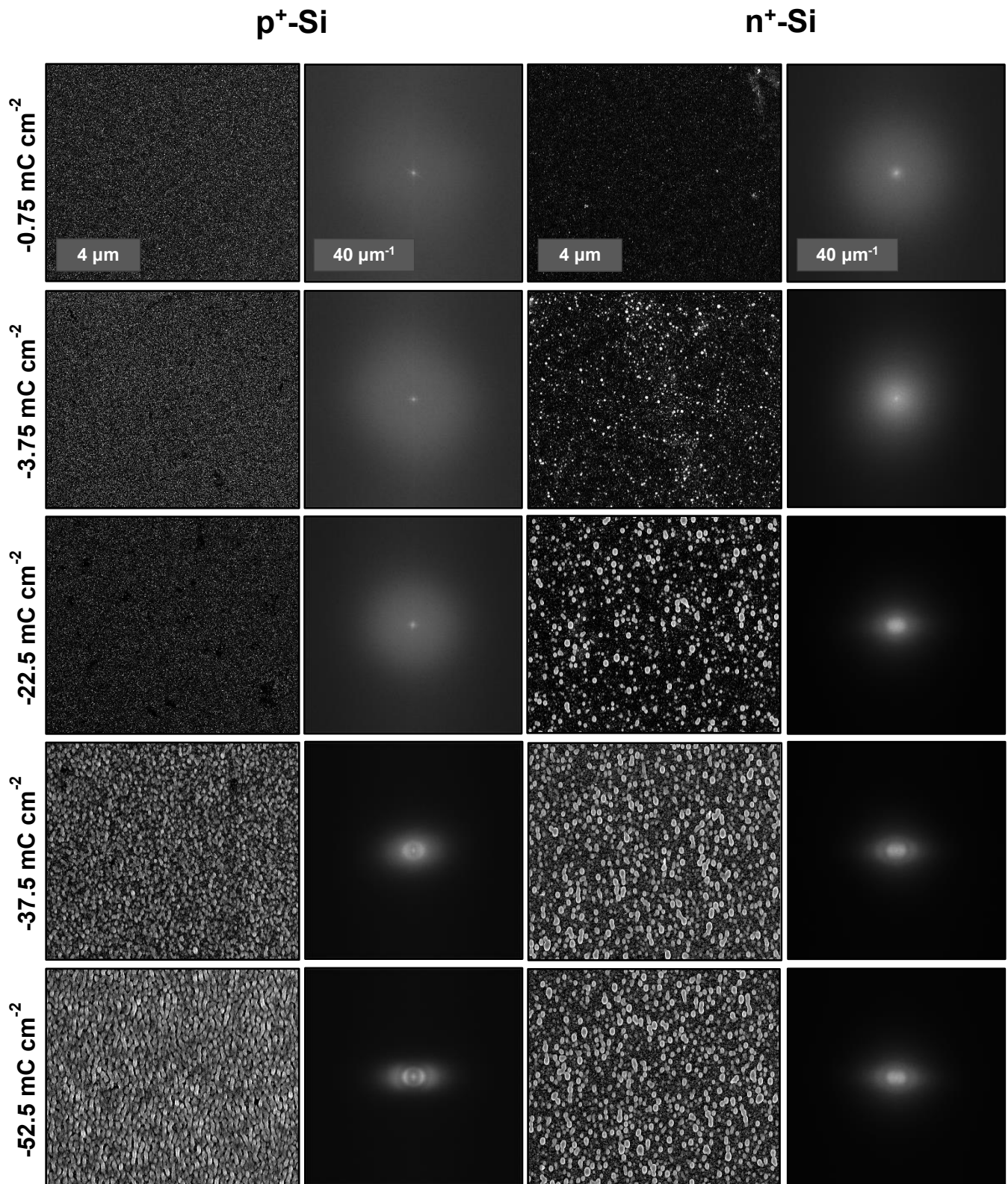**SVII. Electron dispersive X-ray spectroscopy (EDS) compositional analysis**

Figure S10: Compositional data for phototropic Se-Te films deposited on p$^+$-Si, n$^+$-Si, and Au substrates obtained via an electron dispersive X-ray spectroscopy (EDS) module installed on a FEI Nova NanoSEM 450 scanning electron microscope (SEM). The atomic percentage of Se was calculated from the measured Se and Te relative abundance. Average Se atomic percentages for Se-Te deposited on each of the substrates were: p$^+$-Si, 33.2 ± 3.5; n$^+$-Si, 31.3 ± 4.0; Au, 28.7 ± 1.8. The differences in observed Se-Te composition on the various tested substrates were not statistically significant.

SVIII. Extended discussion of Fourier transforms and SEM images in Figure 2

p⁺-Si and n⁺-Si column headers:

p⁺-Si   **n⁺-Si**

-67.5 mC cm⁻²

4 μm   40 μm⁻¹   4 μm   40 μm⁻¹

-187.5 mC cm⁻²

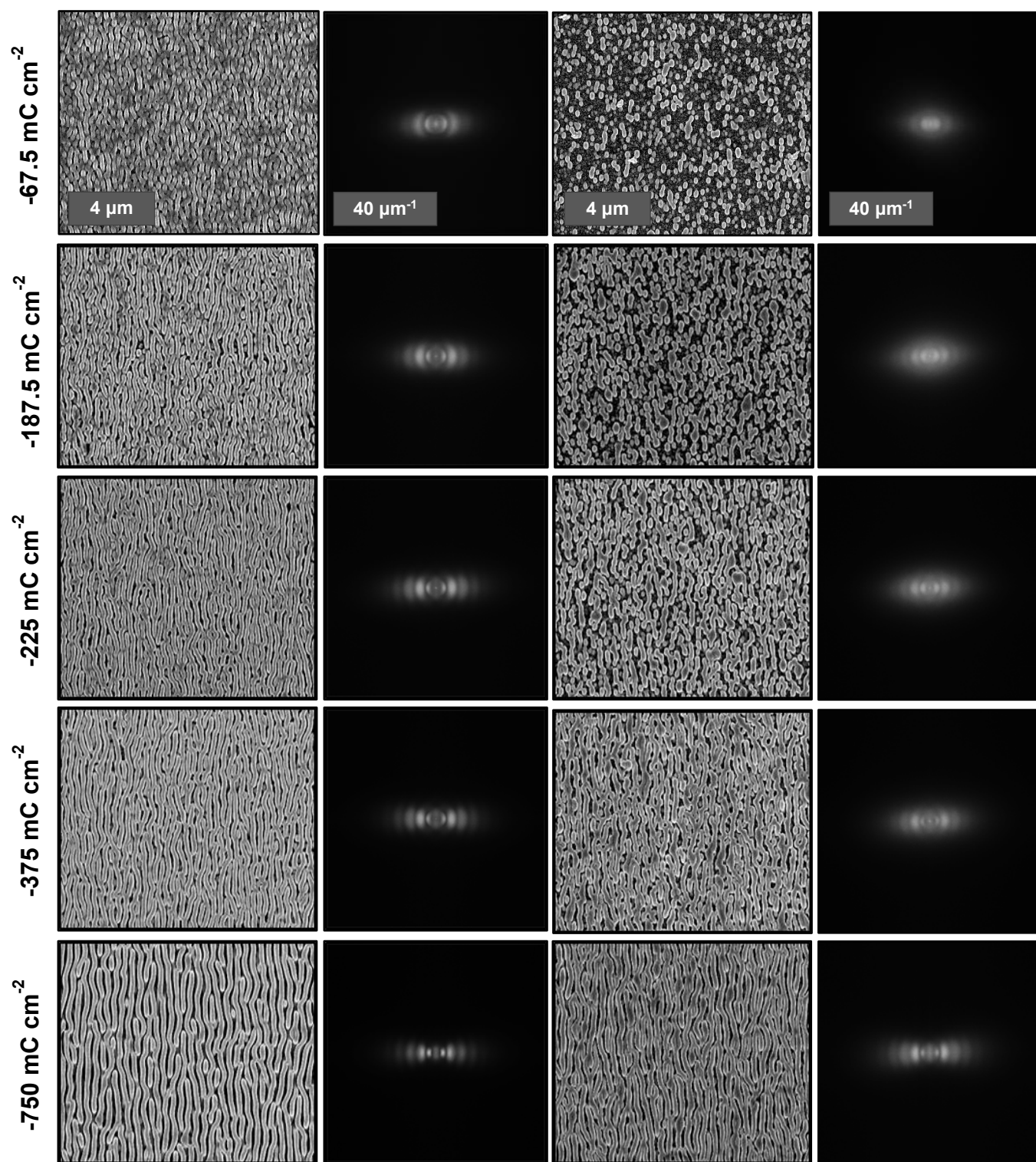-225 mC cm⁻²

-375 mC cm⁻²

-750 mC cm⁻²

Figure S11: SEM images and FT spectra with a higher resolution than those in Figure 2 are provided here with additional discussion. After a charge density of -37.5 mC cm^{-2} was passed on p$^+$-Si and -22.5 mC cm^{-2} was passed on n$^+$-Si, the nucleates adopted a shape that was elongated in the vertical direction, parallel to the axis of polarization. Though the shape of the nucleates was slightly anisotropic, the distribution of nucleates was isotropic. In the FT spectra, the isotropic distribution was indicated by a relatively bright symmetric ring of intensity close to the origin, whereas the elliptical shape of the particles was indicated by an ellipse of intensity, elongated in the horizontal direction, i.e. perpendicular to the axis of polarization. This ellipse of intensity in the FT spectra was observed at relatively higher frequencies in reciprocal space than the features representing the distribution of nucleates. Thus, nucleate dimensions were smaller than the average nucleate spacing at this stage of mass addition on both p$^+$-Si and n$^+$-Si substrates, with relatively smaller nucleate dimensions and spacings observed on p$^+$-Si vs. n$^+$-Si. The elliptical features in the FT spectra were observed for Se-Te deposits on n$^+$-Si until much later stages of mass addition, whereas symmetric horizontal lobes perpendicular to the axis of polarization were observed in FT spectra for deposits on p$^+$-Si at earlier levels of mass addition (starting at -53.5 mC cm^{-2}), indicating a more fully formed lamellar morphology. At later stages of mass addition on n$^+$-Si (-37.5 mC cm^{-2} to -187.5 mC cm^{-2}), vertical spacing between elliptical nucleates was smaller and nucleates converged into longer lamellae. The smaller vertical nucleate spacing was indicated by a progressively higher frequency response in the FT spectra along the axis of polarization at increased levels of mass addition. At the final stage of mass addition (-750 mC cm^{-2}), FT spectra for Se-Te films on p$^+$-Si and n$^+$-Si were similar, though the lower fidelity in films on n$^+$-Si was indicated by broader features with less definition in the FT spectra relative to p$^+$-Si which displayed narrower peaks and more defined high-frequency overtones.

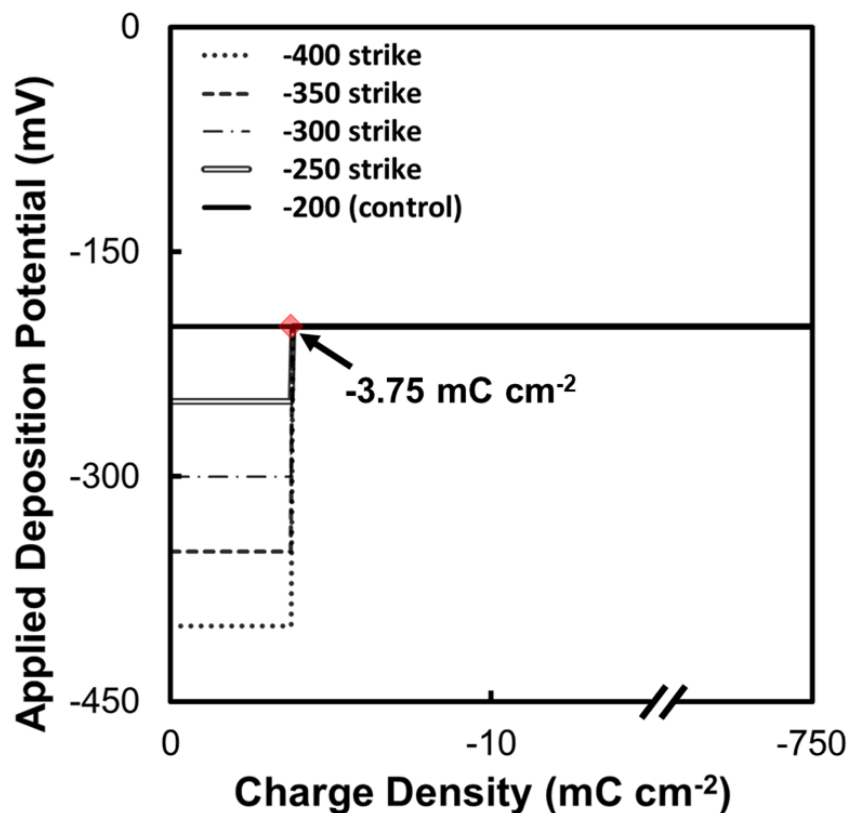**SIX. Graphical representation of striking potential**

Figure S12: Graphical depiction of the experiments in Figure 4-5 demonstrating the procedure followed during variable-potential depositions performed on n^+-Si. Over a total charge density passed of -750 mC cm^{-2}, the initial -3.75 mC cm^{-2} of charge was passed under relatively more negatively applied deposition potentials. For n^+-Si, these "striking" potentials were -400, -350, -300, or -250 mV vs. Ag/AgCl. A control experiment was also performed on n^+-Si in which the entirety of the -750 mC cm^{-2} of charge was passed at -200 mV vs. Ag/AgCl.

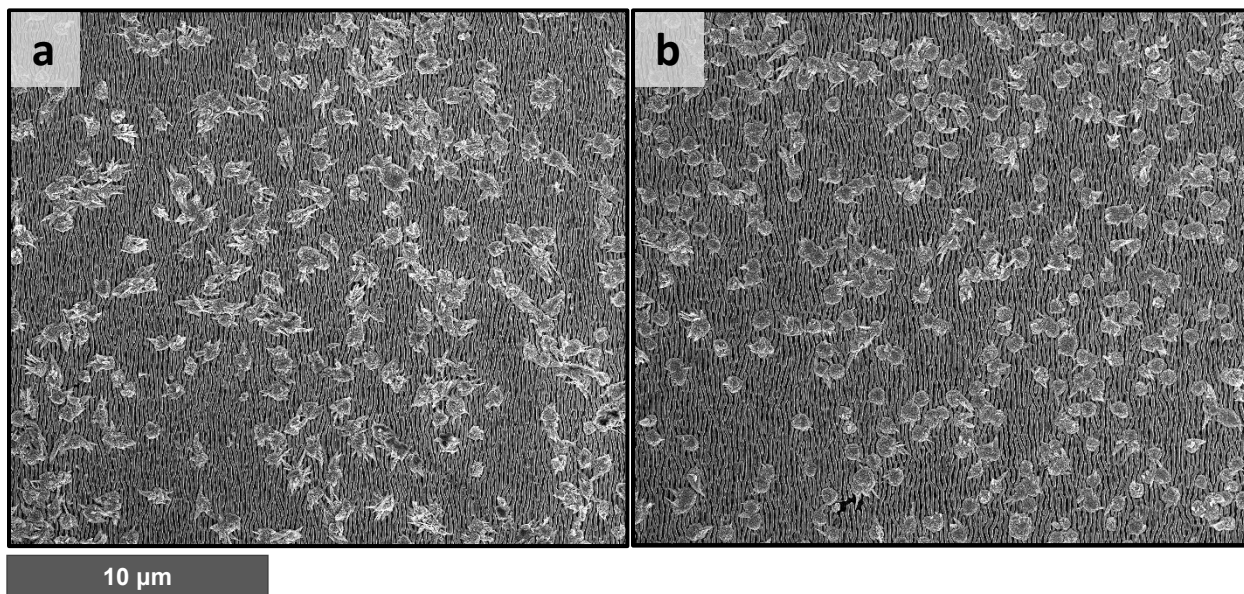**SX. Dark growth during Se-Te electrodeposition on n$^+$-Si**

Figure S13: Low-magnification SEM images of photoelectrodeposited Se-Te films grown on n$^+$-Si at (a) -350 mV and (b) -300 mV vs. Ag/AgCl at a charge density of -750 mC cm^{-2} using vertically polarized $\lambda = 927$ nm illumination at a power density of 53 mW cm^{-2} at a charge density of -3.75 mC cm^{-2}. At these deposition potentials, dark growth was a substantial contribution to the deposited film. These SEM images were obtained at a magnification of 6250 X and a resolution of 4096 x 3536 pixels, which corresponded to ~85.8 pixels μm^{-1}.

SXI. Summary of previous phototropic growth studies

Table S1: Summary of selected publications relating to the phototropic growth of Se-Te

Publication	Summary
Sadtler, B.; Burgos, S. P.; Batara, N. A.; Beardslee, J. A.; Atwater, H. A.; Lewis, N. S., Phototropic growth control of nanoscale pattern formation in photoelectrodeposited Se-Te films. *Proc Natl Acad Sci U S A* **2013,** *110* (49), 19707-12.	• Summary of initial findings, introducing the phenomenon of phototropic growth and the optical growth model showing highly anisotropic lamellar morphology in Se-Te electrodeposits when films are deposited under constant illumination from light with a photon energy larger than the optical bandgap of the Se-Te alloy • Descriptions of the relationships of incident illumination's polarization, wavelength, and incident angle to Se-Te photoelectrodeposit morphology, period, and lamellar alignment
Carim, A. I.; Batara, N. A.; Premkumar, A.; Atwater, H. A.; Lewis, N. S., Self-Optimizing Photoelectrochemical Growth of Nanopatterned Se-Te Films in Response to the Spectral Distribution of Incident Illumination. *Nano Lett* **2015,** *15* (10), 7071-6.	• Series of experiments in which two illumination sources with mutually different wavelengths expand on the relationship between spectral input and resulting lamellar period • Se-Te lamellar period is insensitive to illumination source bandwidth • Se-Te lamellar period is determined entirely by intensity-weighted average wavelength of illumination source, as was determined through dual-beam experiments and substantiated by simulation
Carim, A. I.; Batara, N. A.; Premkumar, A.; Atwater, H. A.; Lewis, N. S., Polarization Control of Morphological Pattern Orientation During Light-Mediated Synthesis of Nanostructured Se-Te Films. *ACS Nano* **2016,** *10* (1), 102-11.	• Series of experiments in which two illumination sources with mutually different linear polarizations expand on the relationship between polarization input and resulting lamellar orientation • Lamellar orientation is dependent on the intensity of each illumination sources in dual-beam experiments, substantiated by simulation
Carim, A. I.; Batara, N. A.; Premkumar, A.; May, R.; Atwater, H. A.; Lewis, N. S., Morphological Expression of the Coherence and Relative Phase of Optical Inputs to the Photoelectrodeposition of Nanopatterned Se-Te Films. *Nano Lett* **2016,** *16* (5), 2963-8.	• For Se-Te films deposited under illumination from two sources with mutually orthogonal (or near-orthogonal) linear polarizations, Se-Te photoelectrodeposit morphology depends on relative phase differences, either coherent or incoherent, over relevant coherence length scales • With coherent illumination between both sources, lamellar morphology oriented along the intensity-weighted axis of polarization (combination of both illumination sources' polarization vectors) is observed • With incoherent illumination between both sources, a mesh-type pattern is observed, similar to the Se-Te photoelectrodeposit morphology for films deposited under unpolarized illumination
Simonoff, E.; Lichterman, M. F.; Papadantonakis, K. M.; Lewis, N. S., Influence of Substrates on the Long-	• Long range order in Se-Te photoelectrodeposits is dependent on growth substrate (p^+-Si or n^+-Si)

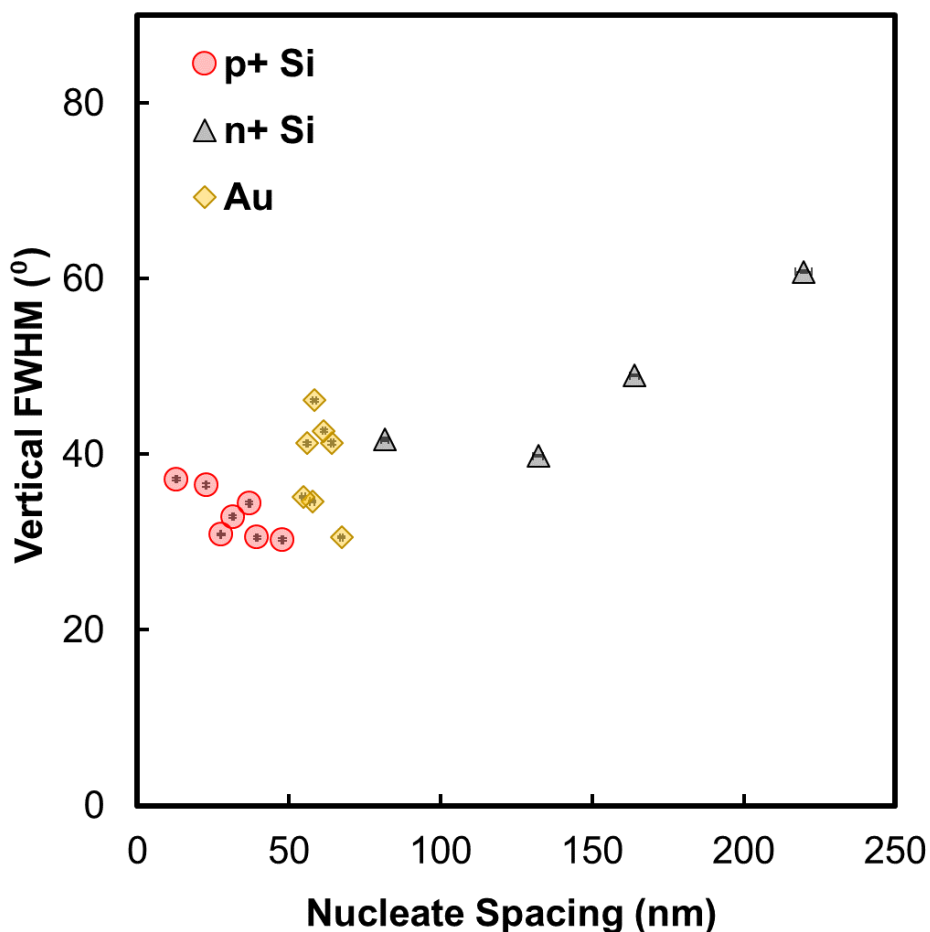| Range Order of Photoelectrodeposited Se-Te Nanostructures. *Nano Lett* **2019,** *19* (2), 1295-1300.	- Se-Te work function alignment with different substrates creates interfacial electrical junctions with different current-voltage behaviors - Straighter, less defective lamellar patterns are observed in Se-Te films photoelectrodeposited on substrates exhibiting a linear, ohmic current-voltage behavior (i.e., p^+-Si) while less straight, more defective lamellar patterns are observed in Se-Te films photoelectrodeposited on substrates exhibiting non-linear current-voltage behavior (i.e., n^+-Si)

SXII. Se-Te on Au substrates

Figure S14: Plot showing the pattern fidelity of phototropically grown Se-Te films described by the vertical (parallel to the axis of polarization) FWHM of the primary peak in the 2D FT of imaged Se-Te films (y-axis) at conditions which produced a given nucleate spacing (x-axis). Points in this plot for p[+]-Si and n[+]-Si are identical to Figure 3 in the main text; this plot also includes points for phototropic Se-Te films deposited on Au substrates. Similar to Figure 3, the films that were analyzed to obtain values for the lamellar period and vertical FWHM were deposited at a charge density of -750 mC cm^{-2}. Vertical FWHM values are paired with corresponding particle spacing values that share applied deposition potentials ranging from -110 to -170 mV vs. Ag/AgCl for Se-Te films deposited on Au substrates. The average fidelity of phototropic Se-Te films on Au

substrates generally agrees with the expected trend of increased fidelity resulting from smaller nucleate spacings.
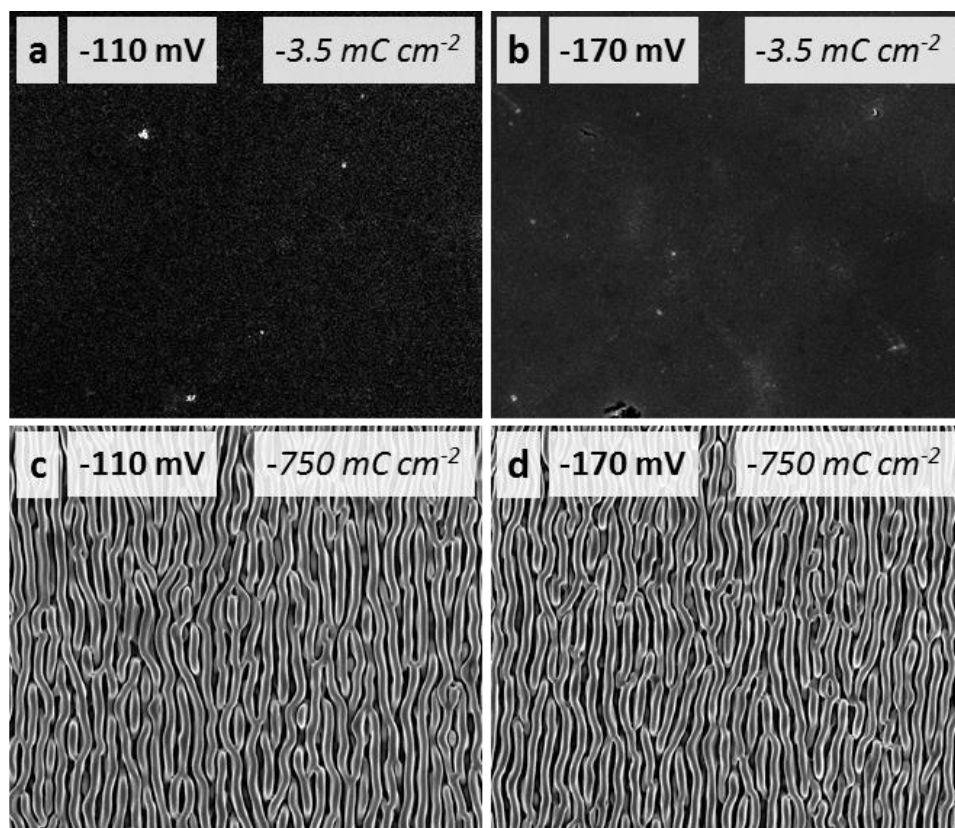
Figure S15: SEM images demonstrating representative phototropic Se-Te films grown on Au substrates at a charge density of (a), (b) -3.5 mC cm-2 and (c), (d) -750 mC cm-2. During the deposition, the Au substrates were illuminated by vertically polarized light from a narrow-band LED with $\lambda = 927$ nm at a power density of 53 mW cm-2. Samples in (a), (c) were deposited at -110 mV vs. Ag/AgCl and samples in (b), (d) were deposited at -170 mV vs Ag/AgCl. The potentials applied constitute the range of the applied deposition potentials in which stable phototropic growth is accessible on Au substrates at the conditions tested. The morphology of Se-Te nucleates is best described as a smooth, thin film. No substantial potential dependence was observed for Se-Te nucleate spacing on Au substrates, as can be observed visually in (a) and (b). Similarly, the results of Fourier analysis of nucleated Se-Te films on Au exhibited a relatively small range of nucleate spacings, as observed in Figure S14.

SXIII. References

1. Simonoff, E.; Lichterman, M. F.; Papadantonakis, K. M.; Lewis, N. S., Influence of Substrates on the Long-Range Order of Photoelectrodeposited Se-Te Nanostructures. *Nano Lett* **2019,** *19* (2), 1295-1300.

2. Finch, C.; Shocksolution_Examples, (2020), GitHub repository, https://github.com/cfinch/Shocksolution_Examples